

# Metamaterial-inspired silicon nanophotonics

Isabelle Staude<sup>1</sup> and Jörg Schilling<sup>2\*</sup>

**The prospect of creating metamaterials with optical properties greatly exceeding the parameter space accessible with natural materials has been inspiring intense research efforts in nanophotonics for more than a decade. Following an era of plasmonic metamaterials, low-loss dielectric nanostructures have recently moved into the focus of metamaterial-related research. This development was mainly triggered by the experimental observation of electric and magnetic multipolar Mie-type resonances in high-refractive-index dielectric nanoparticles. Silicon in particular has emerged as a popular material choice, due to not only its high refractive index and very low absorption losses in the telecom spectral range, but also its paramount technological relevance. This Review overviews recent progress on metamaterial-inspired silicon nanostructures, including Mie-resonant and off-resonant regimes.**

Silicon, like no other material, forms the backbone of modern technology. In addition to its indisputable prevalence in electronic technologies, the field of silicon photonics is also constantly gaining in significance<sup>1,2</sup>. Recent developments in the area of optical metamaterials — artificial materials consisting of designed building blocks arranged on a subwavelength scale — are now offering a new perspective to silicon photonics that reaches beyond classical waveguide-based architectures. For more than a decade, optical metamaterials were almost inevitably associated with plasmonic nanostructures<sup>3–5</sup>. Various metallic nanostructure designs, including split-ring resonators, cut wire antennas and fishnet structures, were employed to create metamaterials and metasurfaces with optical properties that go beyond those of natural materials and their interfaces<sup>4–6</sup>. However, while offering unbeaten performance in subwavelength concentration of light, metallic nanostructures suffer from intrinsic absorption losses at optical frequencies, severely limiting their efficiency.

A way to overcome this problem is offered by all-dielectric nanostructures. Recent research suggests that designed dielectric building blocks provide similar opportunities to their metallic counterparts regarding the design of resonant nanostructures with an optical response tailored by geometry<sup>7,8</sup>. Similar to plasmonic split-ring resonators or related geometries, high-permittivity dielectric nanoparticles provide a strong magnetic response based on the excitation of circular displacement currents inside the dielectric material. In contrast to plasmonic nanoresonators, however, dielectric nanoresonators can exhibit very low absorption losses at near-infrared and visible frequencies. For the implementation of designed dielectric nanostructures, silicon has emerged as the most widely employed material platform to date. At photon energies below its fundamental electronic bandgap at 1.1  $\mu\text{m}$  wavelength, crystalline silicon exhibits a high refractive index and negligible absorption losses. While absorption losses become notable for shorter wavelengths, thus affecting the visible spectral range, their increase is moderate due to the indirect nature of the electronic bandgap. Furthermore, hydrogenated amorphous silicon extends the low-loss regime towards near-visible frequencies due to its blue-shifted bandgap energy. The relevance of silicon for resonant photonic nanostructures is based not only on its linear and nonlinear<sup>9</sup> optical material properties, low cost and mature (nano)fabrication technology, but also on the unique prospects

that silicon-based nanostructures offer in terms of complementary metal-oxide-semiconductor (CMOS) compatibility and for linking to existing integrated photonic architectures.

Here, we review the different concepts of metamaterial-inspired silicon nanostructures. We summarize the main physical effects applied to achieve the desired photonic functionalities and discuss the limitations of silicon metamaterials. As illustrated in Fig. 1, we start the discussion from the subwavelength-sized building blocks (Fig. 1a–c). We then briefly touch on nanoparticle clusters consisting of two or more coupled silicon nanoresonators (Fig. 1d–f) before moving on to metasurfaces, namely two-dimensional arrangements of designed nanoscale silicon building blocks (Fig. 1g,h). Finally, we discuss silicon metamaterials, covering both bulk and waveguide geometries (Fig. 1i–l).

## Individual silicon nanoresonators

The recent renaissance of dielectric metamaterials was triggered by the experimental observation of electric and magnetic multipolar Mie resonances<sup>10</sup> in high-refractive-index dielectric nanoparticles at optical frequencies<sup>11,12</sup>. Mie theory, formulated in 1908 by Gustav Mie, addresses the classical electromagnetic diffraction problem of light scattering by spherical particles<sup>10</sup>. The field scattered by a single isolated dielectric sphere situated in homogeneous surroundings can be expanded into an infinite series of the vector spherical harmonics and fully described by the electric and magnetic Mie coefficients  $a_m$  and  $b_m$  of the expansion. One finds that for high-refractive-index dielectric nanoparticles, the scattering cross-section, which is approximately equal to the extinction cross-section in the case of negligible absorption losses, features a series of peaks corresponding to enhanced scattering at resonance for the different electric and magnetic multipoles. For spherical particles with radius  $r$  and refractive index  $n$  in vacuum, the lowest-order peak corresponds to the magnetic dipole mode (coefficient  $b_1$ ) of the nanosphere and appears at a wavelength of approximately  $\lambda = 2\pi r$ . The next higher-order mode is the electric dipole mode with coefficient  $a_1$  (Fig. 2a). The initial experimental observations of the scattering signatures of these modes at optical frequencies<sup>11,12</sup> were made for silicon nanospheres (Fig. 2b,c), facilitated by the high refractive index and low absorption losses of silicon in this spectral region. An increase of material absorption, for example, through impurities, flattens and broadens the extinction peaks and changes the scattering properties of a silicon nanoparticle<sup>13</sup>.

<sup>1</sup>Institute of Applied Physics, Abbe Center of Photonics, Friedrich Schiller University Jena, 07745 Jena, Germany. <sup>2</sup>Centre for Innovation Competence SiLi-nano, Martin Luther University Halle-Wittenberg, 06120 Halle, Germany. \*e-mail: joerg.schilling@physik.uni-halle.de

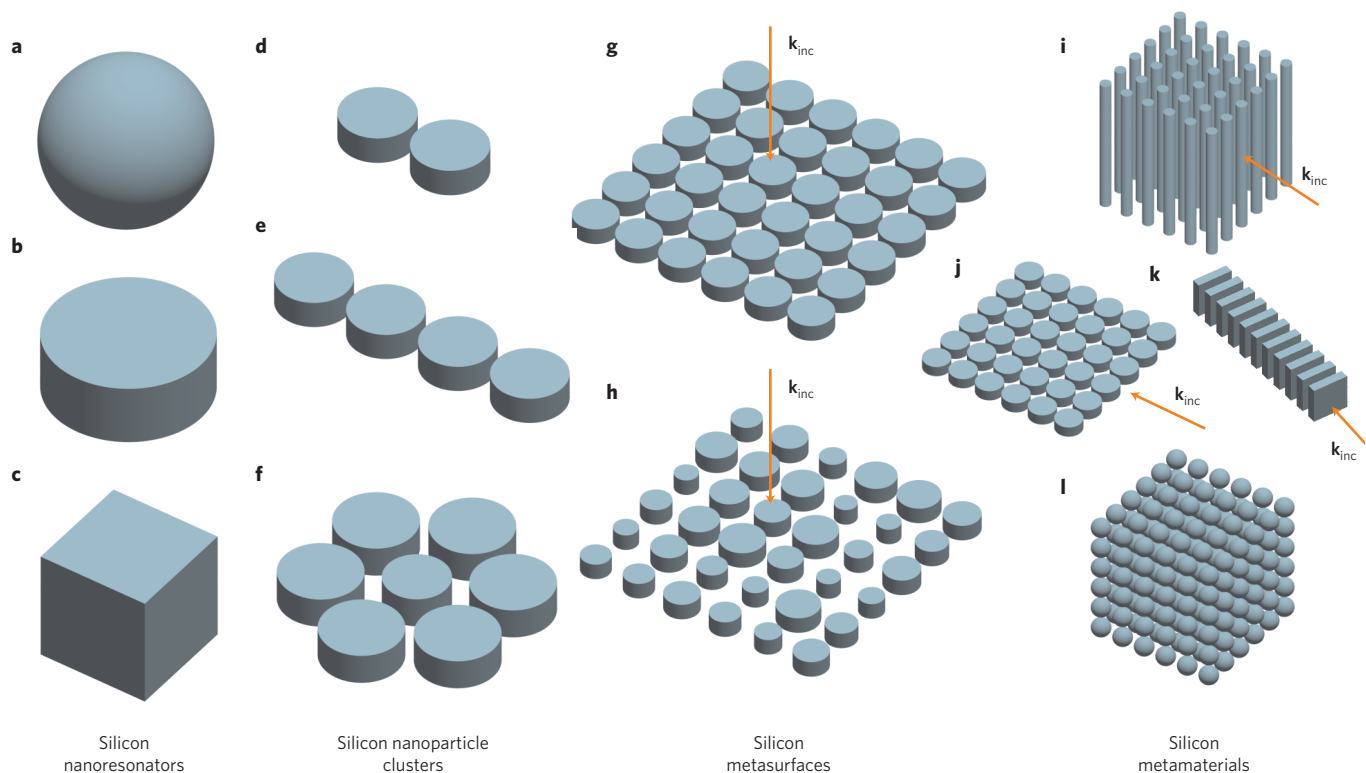


**Figure 1 | From single silicon nanoresonators to functional photonic nanostructures.** **a–c**, Typical silicon nanoresonator geometries providing electric and magnetic dipolar response at optical frequencies. **d–f**, Arranging several silicon nanoresonators in close proximity to form dimers (**d**), chains (**e**) or oligomers (**f**) allows collective and interaction effects to be harnessed. **g,h**, Silicon metasurfaces, typically probed under (near-)normal incidence (wavevector  $k_{\text{inc}}$ ), are obtained by arranging many silicon nanoresonators in a planar fashion. In addition to the functionalities provided by spatially homogeneous silicon metasurfaces (**g**), spatially inhomogeneous metasurfaces (**h**) provide control over the wavefront of a light field. **i–l**, In silicon metamaterials, the light field has a propagating component along the direction in which the individual building blocks are arranged. Typical settings include two-dimensional metamaterials, which are either extended in the third spatial dimension (**i**) or can be realized in a waveguide geometry (**j**), metamaterial strip waveguides (**k**), as well as fully three-dimensional structures (**l**).

The strong electric and magnetic multipolar response of silicon nanoparticles makes them interesting candidates for building blocks of magnetic metamaterials. While Mie theory in its original formulation is strictly valid for spherical nanoparticles only, Mie-type resonances can be observed for many different nanoparticle geometries. For instance, Fig. 2d shows the mode profiles of the electric and magnetic dipole modes of arrayed silicon nanodisks in a homogeneous medium<sup>14</sup>. Importantly, control over the nanoparticle geometry allows for tailoring of the resonances, which was extensively studied, for example, for ellipsoidal, block-shaped and disk-shaped nanoresonators<sup>15–18</sup>, enabling the implementation of desired resonance properties and scattering characteristics of the nanoparticle. One important aspect is the controlled superposition of different multipolar scattering contributions to fulfil the Kerker<sup>16,19</sup> and generalized Kerker<sup>20,21</sup> conditions for zero-backward or almost-zero forward scattering.

More complex geometries allow for targeted resonance shifts by selectively removing material at the locations where a particular mode concentrates its energy<sup>22</sup>. In experiments, the choice of the building block geometry is often determined by the constraints of the respective employed fabrication strategy. Extruded two-dimensional geometries are favoured by standard lithographic approaches, such as electron-beam lithography on silicon thin films, in combination with dry etching. The fabrication of silicon nanoresonators with other shapes requires specialized approaches. For example, silicon nanospheres can be realized by laser printing<sup>23</sup> or via the decomposition of  $\text{Si}_3\text{H}_8$  in supercritical *n*-hexane at high temperature<sup>24</sup>.

While nanostructures featuring Mie-type resonances have clearly been fuelling the recent increase in research attention towards

metamaterial-inspired silicon nanostructures, a resonant response is not always required. In fact, silicon nanostructures operating in the off-resonant regime offer the advantage of broadband response and can also be employed efficiently in various ways to manipulate light fields at will. In this Review, we attempt to provide a balanced overview of both resonant and off-resonant silicon metamaterial-inspired photonic nanostructures.

### Silicon nanoparticle clusters

By combining two or several silicon nanoparticles to form clusters<sup>25–29</sup> (Fig. 1d–f), one can access additional degrees of freedom in the optical response that originate from their mutual interaction. Most prominently, dimers of Mie-resonant silicon nanoresonators were investigated by several groups, mainly with respect to mode hybridization<sup>26</sup> and electric and magnetic field enhancement in the gap between the nanoresonators<sup>27–29</sup> (Fig. 2e). Chains of silicon nanoresonators can create a directional radiation pattern when driven from a localized source, as numerically demonstrated for all-dielectric Yagi–Uda-type nanoantennas<sup>30</sup> (Fig. 2f). Another popular model system for silicon nanoparticle clusters are oligomers (Fig. 2g), which can exhibit Fano resonances originating from the interplay of two or more collective modes<sup>25,31</sup>. Recently, it was furthermore demonstrated that zigzag chains of silicon nanoparticles support topologically protected edge states, which can be selectively excited via control of the handedness of the incident light<sup>32</sup>.

While the study of silicon nanoparticle clusters provides valuable insights into the fundamental mechanisms governing the optical response of silicon nanoparticle ensembles, their use as building

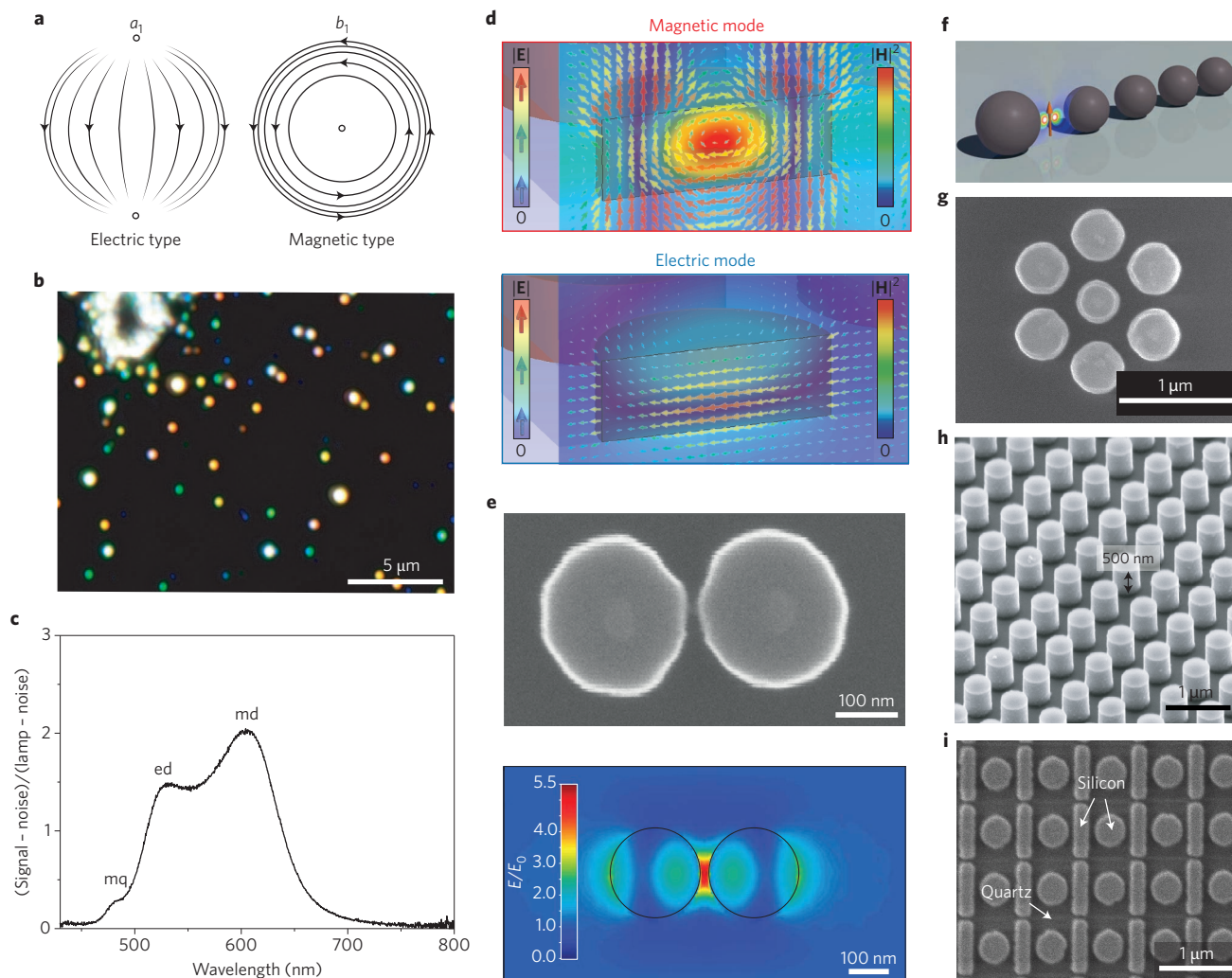


**Figure 2 | Mie-resonant silicon nanostructures.** **a**, Electric field lines (transverse components) of the electric (coefficient  $a_1$ ) and magnetic (coefficient  $b_1$ ) dipolar Mie modes of a spherical particle on an imaginary sphere surrounding the particle, taken from Gustav Mie's original publication<sup>10</sup>. **b**, Real-colour dark-field microscope image of various silicon nanospheres of different size. **c**, Measured reflectance spectrum of an individual silicon nanosphere, with md, ed and mq indicating the magnetic dipole, electric dipole and magnetic quadrupole resonance, respectively<sup>11</sup>. **d**, Typical mode profiles of the dipolar modes of a silicon nanodisk<sup>14</sup>.  $|E|$  is the modulus of the electric field and  $|H|^2$  is the square modulus of the magnetic field. **e**, Scanning electron microscopy (SEM) image of a silicon nanodisk dimer (top) and corresponding calculated electric-field enhancement ( $E/E_0$ ; bottom). **f**, Schematic of a silicon Yagi-Uda nanoantenna for directional emission from a localized electric dipole source<sup>30</sup>. **g**, SEM image of a silicon heptamer supporting magnetic-type Fano resonances<sup>25</sup>. **h**, SEM image of a broadband highly reflective silicon metasurface mirror<sup>33</sup>. **i**, A Fano-resonant silicon metasurface showing strong enhancement of third-harmonic generation<sup>61</sup>. Figure reproduced from: **a**, ref. 10, Wiley; **b,c**, ref. 11, under a Creative Commons licence (<https://creativecommons.org/licenses/by-nc-sa/3.0/>); **d**, ref. 14, Wiley; **e**, ref. 28, Macmillan Publishers Ltd; **f**, ref. 30, OSA; **g**, ref. 25, Wiley; **h**, ref. 33; AIP Publishing LLC; **i**, ref. 62, American Chemical Society.

blocks of metamaterials can be problematic, as their large size hampers a subwavelength arrangement.

### Silicon metasurfaces

Metamaterials require the arrangement of their designed functional building blocks on a subwavelength scale, such that the collective response of the system is dominated by the local optical properties of the individual building blocks instead of by the diffractive modes of the (often periodic) array as in a photonic crystal. While this is difficult to achieve for Mie-resonant silicon metamaterials (see below), the requirements are relaxed for metasurfaces<sup>6</sup>, where the silicon nanoresonators are arranged in a plane and the propagation direction of the light is chosen normal or close to normal to this plane (Fig. 1g,h). For this situation, one can reach a regime where the fundamental Mie-type resonances of a two-dimensional periodic arrangement of silicon building blocks occur at wavelengths beyond the onset of diffraction.

In general, metasurfaces can be used to manipulate the properties of light fields reflected from them or transmitted through them, thereby providing countless possibilities to implement photonic functionality<sup>6</sup>. At the same time, having just nanoscale thickness, they are lightweight and can be made very compact, adding to their high technical relevance. The use of silicon as a constituent material enables high-efficiency devices at frequencies above the electronic band-gap frequency of silicon and may facilitate large-scale production of metasurfaces using existing CMOS technology.

Even when restricting the discussion to spatially homogeneous arrangements of silicon building blocks (Fig. 1g), the range of possible metasurface functionalities is vast. For example, broadband and highly reflective mirrors were realized based on the high reflectivity associated with the electric and magnetic dipole resonances of silicon metasurfaces<sup>33,34</sup> (Fig. 2h). Interestingly, at the magnetic dipole resonance, a dielectric metasurface behaves as a magnetic mirror, which



does not flip the electric field vector<sup>35</sup>. The interplay between the electric and magnetic resonances in silicon metasurfaces was furthermore shown to lead to a large palette of vivid colour impressions spanning the entire visible spectrum<sup>36</sup>. Fano-resonant metasurfaces with sharp spectral features were suggested for high-sensitivity refractive-index and monolayer sensing<sup>37,38</sup>. Also, silicon metasurfaces offer a route towards comprehensive polarization<sup>21,39,40</sup> and dispersion<sup>14</sup> control. Furthermore, the dispersive nature of the optical response of resonant silicon metasurfaces facilitates active tuning of their optical response, paving the way for optical components that can be dynamically controlled or reconfigured. Active tuning of silicon metasurfaces was demonstrated by integration of the metasurface into a liquid crystal cell<sup>41</sup> and by mechanical stretching of the substrate<sup>42</sup>.

The range of possible functionalities of silicon metasurfaces is further increased if inhomogeneous arrangements of designed silicon building blocks in the plane is also allowed for (Fig. 1h), thereby providing a way for tailoring the wavefront of an incident light field. In the past few years, we have witnessed in the literature an explosion of demonstrations of wavefront-shaping silicon metasurface devices, including lenses<sup>43–46</sup>, axicons<sup>43</sup>, blazed gratings<sup>43</sup>, beam splitters<sup>40</sup>, beam deflectors<sup>47,48</sup>, beam shapers<sup>25,39,49,50</sup>, conformal metasurfaces<sup>51</sup>, single<sup>50,52,53</sup> and multicolour<sup>54</sup> holograms, as well as phase masks for microscopy<sup>55</sup>.

In all these applications, the metasurface has to imprint a defined position-dependent phase shift onto the incident light field. Ideally, to implement an arbitrary phase mask, the range of attainable phase-shift values should cover the entire range of  $0$ – $2\pi$ . There are various ways this can be accomplished using nanostructured silicon thin films. We will summarize the most common ones in the following, concentrating on the physical mechanisms employed to generate the desired phase shifts. It is worth noting that several of the presented concepts were first demonstrated with plasmonic nanostructures or using other dielectric materials before being implemented with silicon nanostructures.

A straightforward approach to position-dependent phase control is based on the acquisition of the propagation phase on transmittance through a dielectric layer with a space-variant refractive index. This can be achieved by nanostructuring a silicon film on a deep-sub-wavelength scale, yielding effective refractive index values ranging between air and silicon, depending on the local silicon filling fraction and not relying on resonances. In contrast to conventional diffractive optical elements, which require control of the local film thickness, this concept allows for the realization of a range of phase values with a single lithographic step. Various functional optical devices were realized along these lines, including focusing lenses for near-infrared (Fig. 3a) and terahertz radiation based on silicon posts or subwavelength hole arrays in silicon slabs with spatially varying density or radii<sup>44,56,57</sup>. We discuss more details about effective media in the section ‘Non-resonant bulk silicon metamaterials’, an area where this concept was widely exploited.

Detour phase, another well-known design principle, is based on controlling the phase shift of light diffracted from two adjacent apertures along a given direction via the distance between them. While the concept is inherently dispersive, replacing the conventional apertures by designed silicon nanostructures that act as effective apertures with an engineered dispersion was recently demonstrated to enable more broadband holographic devices<sup>53</sup> (Fig. 3b).

A popular concept for wavefront shaping with photonic metasurfaces relies on the acquisition of a Pancharatnam–Berry phase, a geometric phase originating from space-variant polarization manipulations<sup>43,53,58</sup>. This can be accomplished by tiling a surface with wave-plate elements for which the orientation of the fast axes, described by the in-plane angle  $\theta$ , depends on the in-plane position. Such elements can be realized by silicon nanobeams<sup>43</sup> or nanofins<sup>53</sup> with space-variant orientations (Fig. 3c). For example, an arrangement of half-wave plates with their fast axes orientations following a

function  $\theta(x,y)$ , will transform an incident circularly polarized light beam to a beam of opposite helicity, imprinted with a geometric phase equal to  $\phi_g(x,y) = \pm 2\theta(x,y)$  (ref. 43). Note that metasurfaces utilizing this concept require polarized input light fields.

A method related to the effective-refractive-index approach is transmission through planar arrangements of high-aspect-ratio silicon posts, as it also depends on the acquisition of a spatially varying propagation phase<sup>46</sup>. This concept was demonstrated in nanostructured  $\text{TiO}_2$  films as early as the 1990s<sup>59</sup>. For appropriately chosen feature sizes, such posts function as upright-standing silicon waveguides, with the lateral dimensions of the waveguides determining the propagation constant and the finite vertical dimensions introducing low-quality-factor Fabry–Perot resonator behaviour and allowing for high transmittance efficiency. Alternatively, such posts can also be described as higher-order multipolar Mie-type resonators<sup>21</sup>. Elliptically shaped cross-sections allow for simultaneous control of both phase and polarization, thereby enabling the realization of polarization-sensitive devices and the generation of arbitrary vector beams<sup>50</sup> (Fig. 3d).

Mie-resonant silicon metasurfaces exploit the phase shift of a charge oscillation and the connected scattering field with respect to the phase of the driving field, when the frequency of the exciting field sweeps across the Mie resonance of the building blocks. While for frequencies well below the resonance the charge follows the excitation in phase, at resonance it lags  $\pi/2$  behind and for frequencies well above the resonance it oscillates with  $\pi$  out of phase. An individual resonance provides a phase coverage of only  $\pi$ . Thus, to cover the entire phase range, one needs to combine two or more resonant and/or off-resonant scattering contributions. For example, silicon Mie resonators on a metal back plate can be used<sup>39</sup>, or the scattering contribution from Mie resonators can be interfered with a second contribution of transmitted light<sup>45,48</sup> (Fig. 3e).

A special case of Mie-resonant silicon metasurfaces are Huygens’ metasurfaces<sup>14,47,49,52,60</sup>, where full phase coverage and high transmittance efficiency are achieved by superposition of an electric and a magnetic dipole resonance (Fig. 3f). Silicon Huygens’ metasurfaces can work for arbitrary input polarizations<sup>52,60</sup>.

Which mechanism is the most efficient depends on the specific application requirements. Clearly, when aiming for a broad operation bandwidth, off-resonant structures, dispersion-compensated structures or structures with a high spectral mode density are required. Resonant silicon metasurfaces with a low spectral mode density are strongly dispersive by nature, which makes them more suitable for narrowband devices and active tuning. Another aspect one may consider is the application requirements regarding input polarization, polarization selectivity and spatial dispersion, which can vary strongly among the different concepts. In reality, many demonstrated structures combine elements of two or more of the described approaches.

While all these mentioned functionalities are based on the linear-optical response of the silicon metasurfaces, the high third-order nonlinear susceptibility of silicon also enables the observation of a range of nonlinear optical effects. Making use of the concentration of the electromagnetic fields inside the silicon nanoresonators when exciting a Mie-type resonance, enhancement<sup>61,62</sup> and spectral tailoring<sup>63</sup> of third-harmonic generation was demonstrated in silicon metasurfaces (Fig. 2i). Also, ultrafast nonlinear-optical switching effects in Mie-resonant silicon nanostructures were observed, exploiting the intensity-dependent complex refractive index of silicon through third-order nonlinear effects as well as through free-carrier generation<sup>62,64,65</sup>. For terahertz metasurfaces, one can furthermore make use of the possibility to locally change the silicon material characteristics from dielectric to metallic in a transient fashion by free-carrier generation. For example, by illumination of a silicon wafer with a stripe pattern, a wire grid polarizer for terahertz radiation was demonstrated<sup>66</sup>. Using such a transient metasurface as an external mirror for

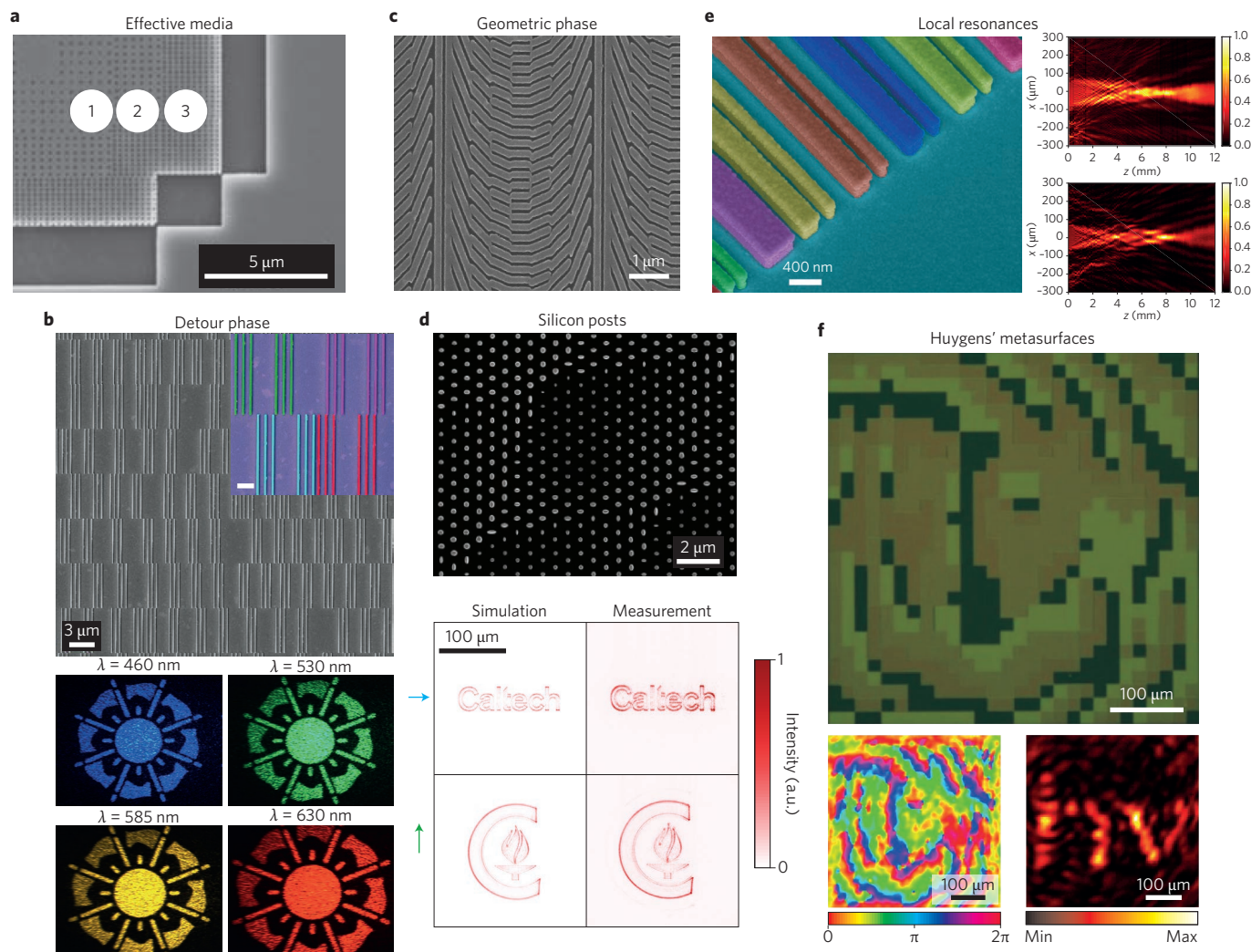


**Figure 3 | Wavefront shaping with silicon metasurfaces.** **a**, SEM image of a metasurface microlens with a locally variable effective refractive index<sup>57</sup>. The numbers indicate regions where different rectangular lattices of nanoholes are used. **b**, SEM image (top) and generated real-colour images (bottom) of a broadband silicon detour-phase metasurface hologram<sup>53</sup>. Inset in top image: close-up SEM image where four pixels are highlighted with different colours. Scale bar, 1  $\mu\text{m}$ . **c**, SEM image of a blazed grating realized by silicon metasurfaces imprinting a space-variant geometric phase<sup>43</sup>. **d**, SEM image (top) of a polarization-sensitive silicon metasurface hologram consisting of silicon posts with spatially varying elliptical cross-section and corresponding measured and calculated generated images for horizontal and vertical linear polarization (bottom)<sup>50</sup>. **e**, Coloured SEM image (left) of an achromatic silicon metasurface lens that employs tailored local resonances; measured (top right) and calculated (bottom right) intensities behind the metasurface<sup>45</sup>. **f**, Light-microscope image (top), retrieved transmittance phase in the metasurface plane (bottom left) and generated image (bottom right) of a holographic element based on the concept of Mie-resonant Huygens' metasurfaces<sup>52</sup>. Figure reproduced from: **a**, ref. 57, OSA; **b**, ref. 53, under a Creative Commons licence (<http://creativecommons.org/licenses/by-nc/4.0/>); **c**, ref. 43, AAAS; **d**, ref. 50, Macmillan Publishers Ltd; **e**, ref. 45, American Chemical Society; **f**, ref. 52, American Chemical Society.

a quantum cascade laser, the laser field amplitude and emission phase could be controlled indirectly by a dynamic change of the illumination pattern<sup>67</sup>.

Another mechanism for nonlinear response from silicon metasurfaces at near-infrared frequencies is offered by connecting the concepts of metasurfaces and silicon-based microelectromechanical systems, where optomechanical coupling can lead to a sizeable optical nonlinearity mediated by mechanical vibration<sup>68</sup>.

Besides the prospect of replacing bulky optical components with ultra-flat optical devices, one of the main driving factors for metasurfaces is the capability of combining several functionalities in a single structure. For instance, wavefront-shaping devices can at the same time control the polarization or be polarization selective, allowing for the generation of any desired spatially varying polarization and phase profiles by a silicon metasurface<sup>50,53</sup>. In addition, as the dispersive properties of silicon metasurfaces can be tailored by the

structure geometry, the concept allows for multiwavelength devices, which can overcome chromatic aberrations<sup>45,46,48,53</sup>. Furthermore, the demonstrated capabilities for resonance tuning in silicon metasurfaces offer a route towards dynamic wavefront control. For example, a silicon metasurface lens with tunable focal length was realized recently based on mechanical stretching of a flexible substrate<sup>69</sup>.

### Silicon metamaterials

While for metasurfaces one typically considers light at normal or near-normal incidence to the nanostructured surface, in metamaterials one is interested in light propagation along the direction(s) in which the building blocks are arranged (Fig. 1i–l). Most commonly, metamaterials have a periodic lattice structure and light propagates along the direction(s) of periodicity. Following this definition, silicon metamaterials include not only fully three-dimensional structures, but also geometries that are nanostructured in one or two dimensions



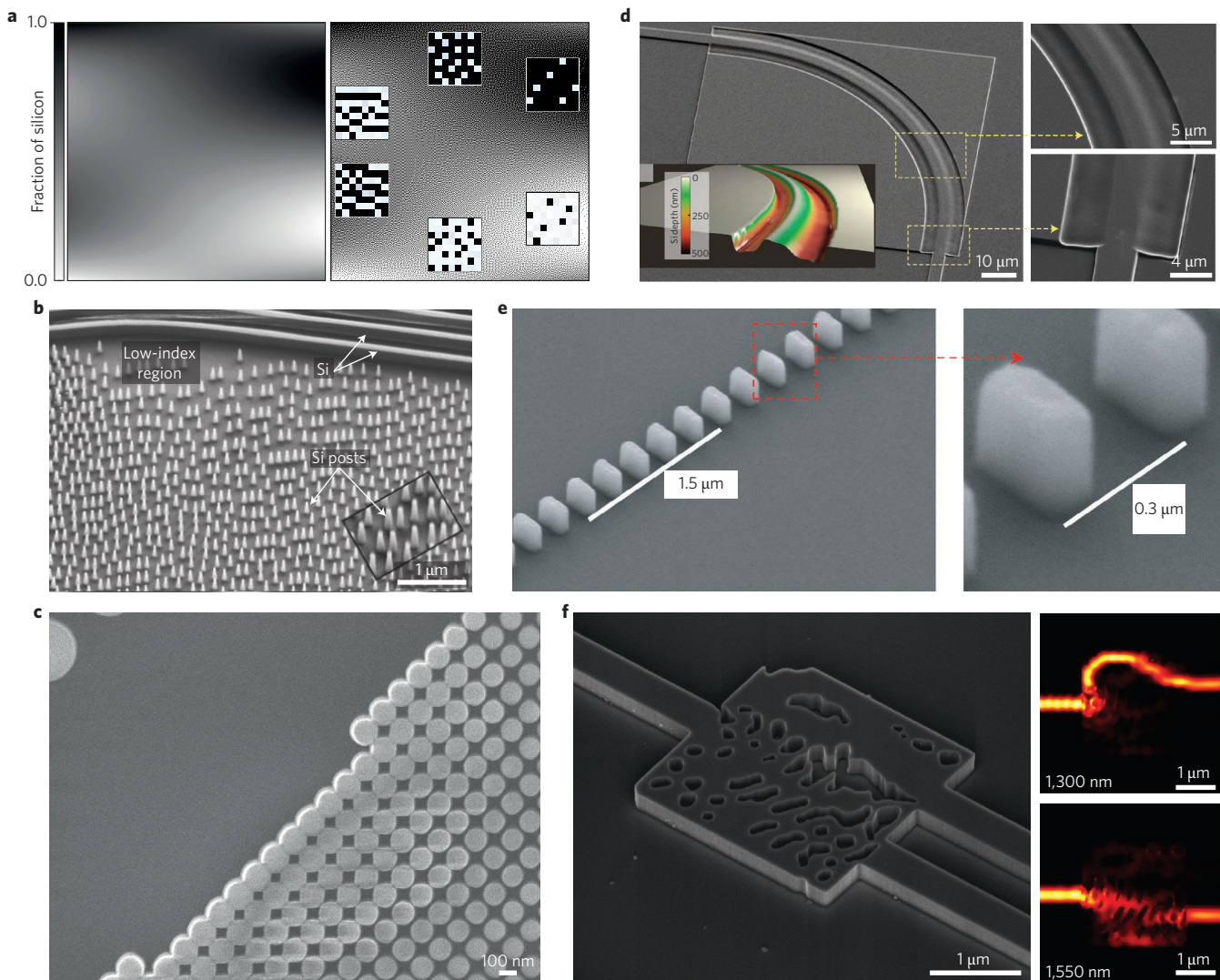


**Figure 4 | Designed graded index silicon structures.** **a**, Dithering technique to transform a continuous index map (left) into an irregular arrangement of individual silicon posts<sup>83</sup>. **b**, SEM image of a carpet cloak based on the dithering technique<sup>82</sup>. **c**, SEM image of a similar carpet cloak based on periodically arranged rods, where the effective index is obtained by locally adjusting the diameter of the rods<sup>84</sup>. **d**, SEM image of a multimode waveguide bend with radially and azimuthally varying height of the waveguide designed by transformation optics<sup>80</sup>. The specific smooth shape of the waveguide minimizes cross-talk between modes. **e**, SEM image of a subwavelength grating waveguide. The distance between neighbouring building blocks is below the Bragg diffraction limit, inhibiting radiation losses<sup>86</sup>. The realized waveguide losses are comparable to usual silicon strip waveguides. **f**, Left: SEM image of a compact and broadband on-chip waveguide demultiplexer as an example of a free-form metamaterial device, whose structure was determined by an inverse-design computer algorithm<sup>92</sup>. Right: the operation of the splitter was observed for the wavelengths 1,300 nm and 1,550 nm. Figure reproduced from: **a**, ref. 83, IOP; **b**, ref. 82, Macmillan Publishers Ltd; **c**, ref. 84, OSA; **d**, ref. 80, Macmillan Publishers Ltd; **e**, ref. 86, OSA; **f**, ref. 92, Macmillan Publishers Ltd.

and infinite (or large) in the remaining dimension(s) as well as nano-structured slab and strip waveguides (Fig. 1i–l).

**Non-resonant bulk silicon metamaterials.** In non-resonant metamaterials, the structure sizes are considerably smaller than the wavelength of operation. Thus, the Mie resonances of these small scattering elements, such as rods, posts or pores, lie well below the wavelength of interest and the distance between the elements is also considerably smaller than half the wavelength, inhibiting any Bragg diffraction within the structure. In this limit, the structures can often be described as simple effective media whose effective refractive index is just a mixture of the refractive indices of its constituents. However, even for non-resonant dielectric structures with very small feature sizes compared with the wavelength, this effective index approximation cannot be taken for granted and

should always be checked carefully, as revealed by a recent study of effective medium approximation breakdown in deeply subwavelength all-dielectric photonic multilayers<sup>70</sup>.

As their main limitation, however, extreme optical properties, such as negative permeability or permittivity, cannot be realized based on this concept and the range of the attainable effective refractive indices is limited by the refractive indices of the parent materials. Nevertheless, the structures have the advantage that they can be almost dispersionless across a large spectral range, allowing the construction of devices that can operate at a wider range of wavelengths.

Porous silicon is an example of a silicon-based effective medium. Fabricated using a (photo)electrochemical etch process, the size of the pores and the overall porosity (air fill factor) depend on doping level and etch current<sup>71</sup>. While macropores with pore diameters on the order of hundreds of nanometres or a few micrometres can be

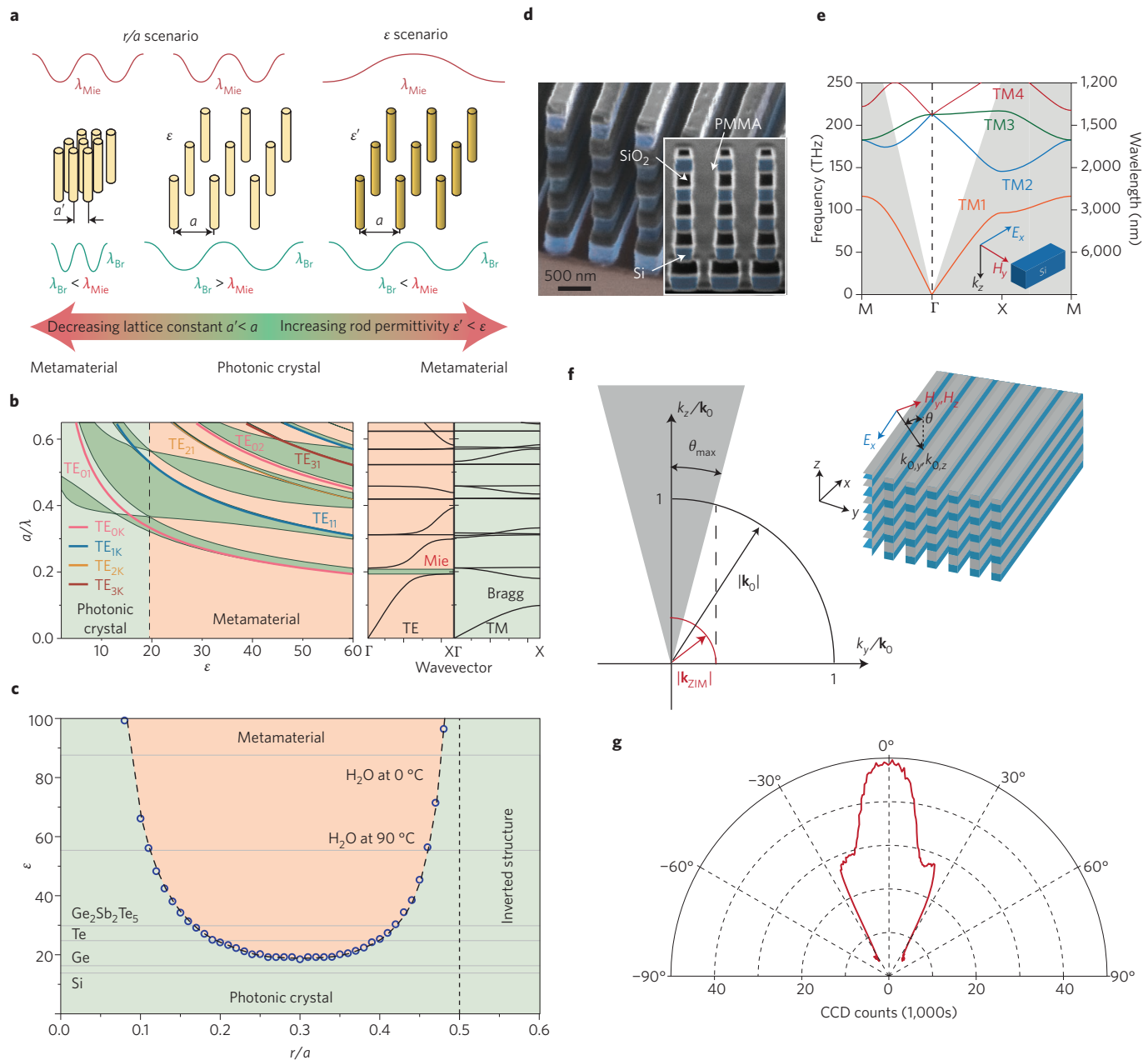


**Figure 5 | Bulk Mie-resonant silicon nanostructures.** **a**, ‘Phase-transition’ between a regular metamaterial and a photonic crystal for a square array of dielectric rods. When the Mie-resonance wavelength is larger than the Bragg-resonance wavelength the structure may be described as a metamaterial. **b**, Transition from a photonic crystal to a metamaterial for increasing permittivity  $\epsilon$  observing transverse electric (TE) and transverse magnetic (TM) polarizations. **c**, Overall ‘phase diagram’ showing for which parameters of  $\epsilon$  and  $r/a$  the structure represents a metamaterial or a photonic crystal. For silicon rods, the structure always represents a photonic crystal. **d**, A two-dimensional silicon rod photonic crystal for the formation of a Dirac cone. PMMA, poly(methylmethacrylate). **e**, The Dirac cone appears for the TM4 band (red) in the dispersion relation. **f**, Light propagating inside the photonic crystal at frequencies slightly above the cone apex experience a very small quasi-effective refractive index and corresponding short Bloch wavevector  $\mathbf{k}_{\text{ZIM}}$  (red arrow), leading to a narrow angular range  $\theta_{\text{max}}$  of outward radiation (grey emission cone).  $\mathbf{k}_0$  represents the wavevector outside the structure and  $k_x$ ,  $k_y$  and  $k_z$  are its three components along the  $x$ ,  $y$  and  $z$  directions. **g**, Experimental observation of the directive emission due to the Dirac cone. CCD, charge-coupled device. Figure reproduced from: **a–c**, ref. 99, Macmillan Publishers Ltd; **d–g**, ref. 101, Macmillan Publishers Ltd.

arranged in perfect periodic regular arrays using a prestructuring technique<sup>72</sup>, nano- and mesoporous silicon exhibits an inherently irregular structure. Considering these structure sizes, macroporous silicon only acts as an effective medium for wavelengths in the mid- and far-infrared<sup>73</sup>, while the small structure sizes of the nano- and mesoporous silicon allow for the realization of effective media in the near-infrared, whose effective refractive index  $n_{\text{eff}}$  can be calculated in good approximation using the well-known Bruggeman formula<sup>74</sup>.

Although silicon represents an optically isotropic material due to its high crystal symmetry, mesoporous silicon exhibits an anisotropic uniaxial effective permittivity tensor. This is caused by the preferential pore etching along the [100] direction causing a corresponding alignment of the optical axis and form birefringence for light incident on the effective medium<sup>75</sup>. With a difference of up to  $\Delta n = 0.2$  between the effective refractive index for ordinary and extraordinary waves, the strength of the effective anisotropy exceeds the values of

classic natural materials such as Iceland spar ( $\Delta n = 0.15$ ). This refractive index difference was used to achieve phase matching for second-harmonic generation in mesoporous silicon<sup>76</sup>.

Since the atomic crystal structure in mesoporous silicon is still the same as in bulk silicon, the absorption of the mesoporous films is negligible for wavelengths above the silicon electronic bandgap. However, the irregular structure of the porous network with pore sizes around 30–50 nm already leads to considerable Rayleigh scattering, which causes an overall extinction of light beams propagating through the mesoporous network<sup>74</sup>.

Recently, mesoporous silicon etching was performed under additional, spatially controlled illumination creating a laterally varying porosity and effective index<sup>77</sup>, allowing the creation of gradient index (GRIN) devices.

The ability to control the refractive index locally over a larger range became especially important with the advent of transformation optics, which provides a mathematical technique to derive a suitable GRIN profile to achieve a desired arbitrary light path in the real world based on a coordinate transformation (mapping) of a simple light propagation in virtual space. Controlling the refractive index landscape in a GRIN material therefore allows the flow of light to be moulded at will. Although this method provides a universal tool to arrive at a permeability  $\mu$  and permittivity  $\epsilon$  landscape that would warrant the desired ray propagation, some of these theoretically derived  $\mu$  and  $\epsilon$  distributions are difficult or impossible to realize — especially when they involve extreme, complex or complicated anisotropic values of  $\mu$  or  $\epsilon$ . These complications are partially alleviated when only the propagation within a plane (two-dimensional) for a single polarization is investigated, and several devices were realized employing locally isotropic GRIN structures in the silicon-on-insulator (SOI) waveguide layer geometry<sup>78–85</sup> (Fig. 1j). To translate a desired refractive index map into a real locally varying effective index landscape, the controlled placement of designed individual subwavelength rods or pores by lithographic techniques represents an important alternative to the irregular mesoporous silicon structures discussed above.

For example, a dithering technique<sup>83</sup> (Fig. 4a) was used to transform a continuously varying ('greyscale') index map into a digitized density map of building blocks with equal size and shape. This leads to arrangements that are locally reminiscent of the structure of quick response (QR) codes (Fig. 4a). Light concentrators, Maxwell's fish-eye lenses<sup>83</sup> and invisibility cloaks<sup>82</sup> were fabricated in this way (Fig. 4b). Similarly, a pore structure was used to realize a planar lens in silicon-waveguide geometry<sup>85</sup>.

Scattering losses originating from the irregular placement of the building blocks can be reduced by placing them on a subwavelength periodic grid and adjusting the local silicon filling fraction by a local variation of their size. Using a hexagonal arrangement of rods or pores, the maximum range of effective refractive indices can be realized<sup>79</sup>. Periodic two-dimensional arrangements of silicon rods or pores were, for example, used to realize carpet cloaks<sup>84</sup> (Fig. 4c) as well as an optical 'Janus' device, which supports different optical functionalities in two propagation directions perpendicular to each other<sup>81</sup>. Furthermore, a planar Lüneburg lens, which focuses a horizontally propagating extended wave onto a spot at the opposite rim of the circular planar lens area, was demonstrated<sup>79</sup>.

Although the characteristic structure sizes are small enough so that Mie or Bragg resonances do not play a role, dispersion is still observable in these planar SOI-based structures, as the finite height of the building blocks introduces horizontal waveguide dispersion to the structures. This becomes crucial when longer wavelengths (for example,  $\lambda > 1,550$  nm) are considered, which lie beyond the cut-off of the horizontal waveguide mode and therefore lead to substantial radiation losses<sup>83</sup>. Alternatively, this waveguide dispersion can be used intentionally to create a smoothly varying effective refractive index within the plane by locally controlling the thickness (height) of the waveguide layer. Using a greyscale mask for etching, a Lüneburg

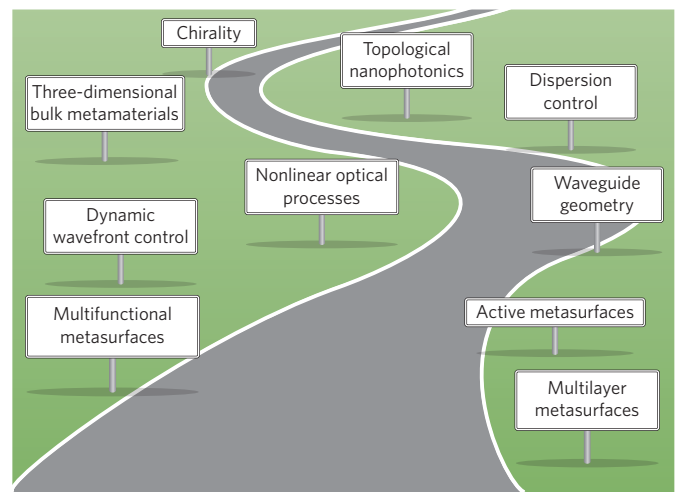


**Figure 6 | The possible road ahead for metamaterial-inspired silicon nanostructures.**

lens was implemented by a continuously varying index profile<sup>77</sup> and an optimized height profile for multimode strip waveguide bends was realized (Fig. 4d), minimizing the cross-talk between the modes in the bend and relaxing the requirements for single-mode transmission on-chip in this way<sup>80</sup>.

Besides the use of two-dimensional metamaterial slabs for full-scale planar transformation optics devices, periodic subwavelength-sized structures were also used in simpler geometries. A chain of 300-nm-wide and 150-nm-thick silicon posts with a period of 300 nm was prepared from SOI substrates and represents a sub-wavelength grating waveguide (Fig. 4e). Since the period is below the distance required for the onset of Bragg diffraction, the waveguide exhibits an effective mode index in the near-infrared that depends on the duty cycle of the posts. A low 2.1 dB cm<sup>-1</sup> loss of the waveguide is comparable to usual silicon-strip waveguides<sup>86</sup>. Furthermore, mode converters<sup>87</sup> and waveguide crossings with low cross-talk and only minimal loss were created<sup>88</sup>. A recent review of the use of subwavelength grating structures for refractive-index engineering in silicon photonics, including fully etched, broadband grating couplers as well as directive and multimode interference couplers, can be found in ref. 89.

Apart from these analytical-based strategies, different numerical algorithms were developed, which allow a computer to design and optimize free-form metamaterial structures to fulfil specific purposes. These algorithms are based on an inverse-design strategy, where the desired functionality enters the algorithm as an input. In this way, compact, on-chip integrated mode converters<sup>90</sup>, waveguide splitters<sup>91</sup>, broadband wavelength demultiplexers<sup>92</sup> and polarization beam-splitters<sup>93</sup> were demonstrated (Fig. 4f).

The use of the SOI platform to test and realize GRIN devices has resulted in many successful experimental implementations and more theoretical proposals are still waiting to be realized<sup>94</sup>. In contrast, the realization of bulk silicon metamaterials with a custom-engineered graded refractive index in all three dimensions faces several fundamental challenges. Most importantly, in three dimensions, transformation optics frequently leads to extreme or anisotropic permittivity or permeability requirements, which cannot be fulfilled by the GRIN structures. For more complex permittivity and permeability landscapes, certain additional opportunities are offered by metamaterials composed of Mie-resonant building blocks.

**Resonant bulk silicon nanostructures.** Despite the successful deployment of silicon nanoresonators as building blocks of metasurfaces, the creation of Mie-resonant bulk metamaterials faces several



fundamental limitations. While analytical expressions for the effective permittivity and permeability of composite materials consisting of Mie-resonant particles were derived soon after the publication of Mie's original paper<sup>95,96</sup> and later revisited<sup>97,98</sup>, they can only yield meaningful results if the wavelength of light is clearly larger than the typical distance between the Mie-resonant building blocks. Thus, to create a periodic metamaterial with homogenized properties, such as negative permittivity and/or permeability, zero permittivity or negligible effective refractive index, the Mie resonances have to occur at frequencies below the first photonic bandgaps created by the Bragg resonances. This usually requires high-refractive-index nanoresonators embedded in a low-refractive-index matrix. This interplay between the size of the nanoresonators, their dielectric constant and the lattice periodicity was recently investigated in detail for the case of square arrays of dielectric rods in air<sup>99</sup> (Fig. 5a).

Starting from a relatively large periodicity and moderate dielectric constant of the rods, either the periodicity was reduced to push the Bragg resonance to shorter wavelengths  $\lambda_{\text{Br}}$ , or the dielectric constant of the rods was increased to shift the Mie resonance  $\lambda_{\text{Mie}}$  to longer wavelengths to enter the metamaterial regime ( $\lambda_{\text{Br}} < \lambda_{\text{Mie}}$ ). For the opposite case ( $\lambda_{\text{Br}} > \lambda_{\text{Mie}}$ ), the Mie resonance will mix with higher Bragg resonances and the structure becomes a photonic crystal. The gap map shown in Fig. 5b for increasing  $\epsilon$  shows the 'phase transition' between a metamaterial and a photonic crystal, when the gap connected to the TE01 Mie resonance crosses below the first Bragg gap. In Fig. 5c, the phase diagram for varying  $\epsilon$  and  $r/a$  values (rod radius/period ratio) of the structure is given. From this diagram, it can be concluded that a square array of silicon rods will always represent a photonic crystal, since for all  $r/a$  values, the Bragg gap is positioned at longer wavelengths than the Mie resonance. Enlarging the rod diameter to shift the Mie resonance to longer wavelengths is not sufficient to enter the metamaterial regime, as the Bragg gap also shifts to longer wavelengths due to the increasing overall effective index of the structure ( $\lambda_{\text{Br}} \approx 2an_{\text{eff}}$ , where  $a$  is the period and  $n_{\text{eff}}$  is the effective refractive index of the structure)<sup>99</sup>.

Although these results seem to impede the realization of bulk silicon-based Mie-resonant metamaterials, metamaterial properties can be supported by periodic silicon nanostructures owing, for example, to the formation of Dirac cones at the  $\Gamma$  point at finite frequencies<sup>100</sup>. This happens when two photonic bands exhibiting linear or nearly linear dispersion touch each other at the  $\Gamma$  point forming a sharp cone with its apex directly at the  $\Gamma$  point. In this case, a quasi-effective refractive index can be defined for the Bloch wavevector. Such a structure was created by depositing several layers of silicon rods separated by low-refractive-index dielectric spacers<sup>101</sup> (Fig. 5d). The photonic band structure exhibits the Dirac cone for the TM4 band (Fig. 5e; red). Since the Bloch wavevector is small in the proximity of the  $\Gamma$  point, the angular range of outside waves that can be excited by these near- $\Gamma$  Bloch waves is small (Fig. 5f). This results in a narrow emission cone for luminescent quantum dots, which are incorporated inside the three-dimensional structure (Fig. 5g). More recently, a two-dimensional periodic structure exhibiting a Dirac cone for in-plane propagating light was developed and radiation emerging perpendicular from the facets of a prism was observed, indicating that the structure supports a zero quasi-effective refractive index<sup>102</sup>. In general, the approximation of the band structure dispersion by a quasi-effective refractive index is only valid over a relatively narrow spectral range, where only a single band forms the Dirac cone.

As another fundamental limitation of Mie-resonant bulk metamaterials, it is important to note that when Mie-resonant elements are arranged in a disordered array, diffuse resonant scattering becomes crucial and dominates the overall light propagation through the structure. Scattering losses and the corresponding extinction are then considerable and the description of the structure by simple homogenized effective optical constants becomes impossible<sup>103</sup>.

## Outlook

Despite intense research efforts into metamaterial-inspired silicon nanophotonics in the past few years, many aspects remain to be explored in detail. In Fig. 6, we illustrate which research topics we expect to develop rapidly in the not-too-distant future. Mie resonances will be an essential element in this development since they allow phase and dispersion control with negligible Ohmic losses as well as the local resonant enhancement of the light field.

Metasurfaces will continue to be a hot topic both for future beam-shaping devices, as well as a test platform for new concepts, such as multifunctional metasurfaces combining wavefront control with other metasurface functionalities, for example, local control of polarization<sup>50</sup> or nonlinear optical response. Also, a rapid development of actively tunable devices can be expected. In general, realizations of dynamic wavefront control with silicon metasurfaces are still sparse<sup>69</sup>, and it will be up to future research to explore how the previously investigated resonance tuning mechanisms<sup>41,69</sup> can be employed to this end. In this respect, the combination of the silicon building blocks with electro-optic or thermo-optic materials in hybrid devices also represents a viable strategy.

Another important task will be to investigate and exploit the Mie-resonant enhancement of light-matter interactions. Due to the field concentration inside the Mie-resonant building blocks, absorption in the silicon can be considerably enhanced, which could be exploited for boosting the efficiency of silicon-based optoelectronic devices, such as solar cells and photodetectors. This strategy may furthermore provide additional functionalities for silicon detectors, such as a polarization-sensitive or spectrally selective response. Similarly, the manipulation of spontaneous emission from luminescence centres by silicon Mie resonators will be of interest. Active metasurfaces could then be employed to create novel light sources capable of generating light fields with precisely tailored polarization as well as spectrally and directionally controlled emission properties. Interestingly, this possibility is not limited to common electric-dipole emitters, but may also enhance spontaneous emission through magnetic dipolar transitions<sup>104</sup>.

Furthermore, the capability to tailor the dispersion of a Mie-resonant silicon nanostructure could be exploited for manipulating the temporal properties of laser pulses. Controlling dispersion as a function of in-plane position on a silicon metasurface may even allow its spatiotemporal optical response to be engineered. Due to the high transmission that can be achieved in the near-infrared spectral range, the stacking of several metasurfaces for a stronger accumulated effect is possible<sup>14</sup>. The opportunity to combine two or more layers to form multilayer metasurfaces widens the engineering options for more complex and aberration-controlled optical systems. For example, very recently, a planar camera was realized using two silicon metasurfaces<sup>105</sup>.

Besides the development of metasurfaces, the incorporation of metamaterial concepts into a planar waveguide geometry is expected to continue. Starting from the subwavelength grating waveguides<sup>86,88,106</sup>, the application of further successful concepts, such as directional scattering, sharp Fano resonances and active tuning of resonant photonic properties, which so far have been mainly studied in silicon metasurfaces, could enable a new class of very compact low-loss devices for all-silicon on-chip photonic circuitry — such as compact sensors, switches and modulators. The alignment of Mie-resonant building blocks in chains may also lead to ultimate flexibility in waveguide dispersion engineering. Combined with the field enhancement in Mie-resonant structures, this also offers favourable conditions for the enhancement of nonlinear optical processes. Exploiting the large third-order nonlinear susceptibility,  $\chi^{(3)}$ , of silicon, efficient opto-optical switching, frequency conversion via four-wave mixing, as well as spectral broadening based on self- and cross-phase modulation might be envisaged. Even  $\chi^{(2)}$  processes, such as second-harmonic generation, could be enhanced in silicon Mie resonators when the inversion symmetry

of the crystal lattice of silicon is broken, for example, by an applied inhomogeneous strain<sup>107</sup>. The use of metamaterial-inspired silicon nanostructures for nonlinear processes will be especially effective in the mid-infrared spectral region for  $\lambda > 2.3 \mu\text{m}$  as then the nonlinear two-photon absorption of silicon is absent.

Beyond the planar extended waveguide geometry, the future of truly three-dimensional bulk silicon metamaterials is more uncertain. In addition to the discussed fundamental obstacles in obtaining metamaterial behaviour in Mie-resonant bulk silicon nanostructures<sup>99,103</sup>, arbitrary three-dimensional silicon nanostructures are also extremely difficult to fabricate. Nevertheless, the study of three-dimensional metamaterial-inspired arrangements of silicon nanoparticles exhibiting electric and magnetic Mie-type resonances is interesting from a fundamental perspective. It could stimulate advances in various fields ranging from three-dimensional nanofabrication technology to chiral or bianisotropic silicon nanostructures and even silicon-based topological nanophotonics<sup>108</sup>. Also, media or suspensions<sup>24</sup> consisting of silicon nanoparticles exhibiting, for example, unusual directional scattering properties in a solid or liquid matrix are of interest.

It is worth noting that other materials, in particular III–V semiconductors, offer similar opportunities to silicon for Mie-resonant devices while providing stronger light–matter interactions and nonlinear response due to their direct electronic bandgap and non-centrosymmetric lattice<sup>109</sup>. However, the advantage of silicon lies in the key role that it already plays both in electronics and on-chip photonics, making silicon metamaterial-inspired solutions highly relevant for applications.

Received 16 September 2016; accepted 28 February 2017;  
published online 28 April 2017

## References

- Dong, P., Chen, Y., Duan, G. & Neilson, D. T. Silicon photonic devices and integrated circuits. *Nanophotonics* **3**, 215–228 (2014).
- Reed, G. T. *Silicon Photonics: The State of the Art* (Wiley-Interscience, 2008).
- Linden, S. *et al.* Magnetic response of metamaterials at 100 terahertz. *Science* **306**, 1351–1353 (2004).
- Zhang, S. *et al.* Experimental demonstration of near-infrared negative-index metamaterials. *Phys. Rev. Lett.* **95**, 137404 (2005).
- Shalaev, V. M. *et al.* Negative index of refraction in optical metamaterials. *Opt. Lett.* **30**, 3356–3358 (2005).
- Yu, N. & Capasso, F. Flat optics with designer metasurfaces. *Nat. Mater.* **13**, 139–150 (2014).
- Zhao, Q., Zhou, J., Zhang, F. & Lippens, D. Mie resonance-based dielectric metamaterials. *Mater. Today* **12**, 60–69 (December, 2009).
- Jahani, S. & Jacob, Z. All-dielectric metamaterials. *Nat. Nanotech.* **11**, 23–36 (2016).
- Leuthold, J., Koos, C. & Freude, W. Nonlinear silicon photonics. *Nat. Photon.* **4**, 535–544 (2010).
- Mie, G. *Beiträge zur Optik trüber Medien, speziell kolloidaler Metallösungen*. *Ann. Phys.* **25**, 377–445 (1908).
- Kuznetsov, A. I., Miroshnichenko, A. E., Fu, Y. H., Zhang, J. & Luk'yanchuk, B. Magnetic light. *Sci. Rep.* **2**, 492 (2012).
- Evlyukhin, A. B. *et al.* Demonstration of magnetic dipole resonances of dielectric nanospheres in the visible region. *Nano Lett.* **10**, 3749–3755 (2012).
- Sanz, J. M. *et al.* Influence of pollutants in the magneto-dielectric response of silicon nanoparticles. *Opt. Lett.* **39**, 3142–3144 (2014).
- Decker, M. *et al.* High-efficiency dielectric Huygens' surfaces. *Adv. Opt. Mater.* **3**, 813–820 (2015).
- Evlyukhin, A. B., Reinhardt, C. & Chichkov, B. N. Multipole light scattering by nonspherical nanoparticles in the discrete dipole approximation. *Phys. Rev. B* **84**, 235429 (2011).
- Fu, Y. H., Kuznetsov, A. I., Miroshnichenko, A. E., Yu, Y. F. & Luk'yanchuk, B. Directional visible light scattering by silicon nanoparticles. *Nat. Commun.* **4**, 1527 (2013).
- Staudte, I. *et al.* Tailoring directional scattering through magnetic and electric resonances in subwavelength silicon nanodisks. *ACS Nano* **7**, 7824–7832 (2013).
- Ee, H., Kang, J., Brongersma, M. L. & Seo, M. Shape-dependent light scattering properties of subwavelength silicon nanoblocks. *Nano Lett.* **15**, 1759–1765 (2015).
- Kerker, M., Wang, D. & Giles, C. L. Electromagnetic scattering by magnetic spheres. *J. Opt. Soc. Am.* **73**, 765–767 (1983).
- Alaee, R., Filter, R., Lehr, D., Lederer, F. & Rockstuhl, C. A generalized Kerker condition for highly directive nanoantennas. *Opt. Lett.* **40**, 2645–2648 (2015).
- Kruk, S. *et al.* Broadband highly-efficient dielectric metadevices for polarization control. *APL Photon.* **1**, 30801 (2016).
- Campione, S., Basilio, L. I., Warne, L. K. & Sinclair, M. B. Tailoring dielectric resonator geometries for directional scattering and Huygens' metasurfaces. *Opt. Express* **23**, 2293–2307 (2015).
- Zywietz, U., Evlyukhin, A. B., Reinhardt, C. & Chichkov, B. N. Laser printing of silicon nanoparticles with resonant optical electric and magnetic responses. *Nat. Commun.* **5**, 3402 (2014).
- Shi, L. *et al.* Monodisperse silicon nanocavities and photonic crystals with magnetic response in the optical region. *Nat. Commun.* **4**, 1904 (2013).
- Chong, K. E. *et al.* Observation of Fano resonances in all-dielectric nanoparticle oligomers. *Small* **10**, 1985–1990 (2014).
- Zywietz, U. *et al.* Electromagnetic resonances of silicon nanoparticle dimers in the visible. *ACS Photon.* **2**, 913–920 (2015).
- Bakker, R. M. *et al.* Magnetic and electric hotspots with silicon nanodimers. *Nano Lett.* **15**, 2137–2142 (2015).
- Caldarola, M. *et al.* Non-plasmonic nanoantennas for surface enhanced spectroscopies with ultra-low heat conversion. *Nat. Commun.* **6**, 7915 (2015).
- van de Groep, J., Coenen, T., Mann, S. A. & Polman, A. Direct imaging of hybridized eigenmodes in coupled silicon nanoparticles. *Optica* **3**, 93–99 (2016).
- Krasnok, A. E., Miroshnichenko, A. E., Belov, P. A. & Kivshar, Y. S. All-dielectric optical nanoantennas. *Opt. Express* **20**, 20599–20604 (2012).
- Miroshnichenko, A. E. & Kivshar, Y. S. Fano resonances in all-dielectric oligomers. *Nano Lett.* **12**, 6459–6463 (2012).
- Slobozhanyuk, A. P. *et al.* Enhanced photonic spin Hall effect with subwavelength topological edge states. *Laser Photon. Rev.* **10**, 656–664 (2016).
- Moitra, P., Slovick, B. A., Yu, Z. G., Krishnamurthy, S. & Valentine, J. Experimental demonstration of a broadband all-dielectric metamaterial perfect reflector. *Appl. Phys. Lett.* **104**, 171102 (2014).
- Moitra, P. *et al.* Large-scale all-dielectric metamaterial perfect reflectors. *ACS Photon.* **2**, 692–698 (2015).
- Liu, S. *et al.* Optical magnetic mirrors without metals. *Optica* **1**, 250–256 (2014).
- Proust, J., Gallas, B., Ozerov, I. & Bonod, N. All-dielectric colored metasurfaces with silicon Mie resonators. *ACS Nano* **10**, 7761–7767 (2016).
- Yang, Y., Kravchenko, I. I., Briggs, D. P. & Valentine, J. All dielectric metasurfaces analogue of electromagnetically induced transparency. *Nat. Commun.* **5**, 5753 (2014).
- Wu, C. *et al.* Spectrally selective chiral silicon metasurfaces based on infrared Fano resonances. *Nat. Commun.* **5**, 3892 (2014).
- Yang, Y. *et al.* Dielectric meta-reflectarray for broadband linear polarization conversion and optical vortex generation. *Nano Lett.* **14**, 1394–1399 (2014).
- Khorasaninejad, M. K., Zhu, W. Z. & Crozier, K. B. Efficient polarization beam splitter pixels based on a dielectric metasurface. *Optica* **2**, 376–382 (2015).
- Sautter, J. *et al.* Active tuning of all-dielectric metasurfaces. *ACS Nano* **9**, 4308–4315 (2015).
- Kamali, S. M., Arbabi, E., Arbabi, A., Horie, Y. & Faraon, A. Highly tunable elastic dielectric metasurface lenses. *Laser Photon. Rev.* **10**, 1002–1008 (2016).
- Lin, D., Fan, P., Hasman, E. & Brongersma, M. L. Dielectric gradient metasurface optical elements. *Science* **345**, 298–302 (2014).
- West, P. R. *et al.* All-dielectric subwavelength metasurface focusing lens. *Opt. Express* **22**, 26212–26221 (2014).
- Khorasaninejad, M. *et al.* Achromatic metasurface lens at telecommunication wavelengths. *Nano Lett.* **15**, 5358–5362 (2015).
- Arbabi, E., Arbabi, A., Kamali, S. M., Horie, Y. & Faraon, A. Multiwavelength polarization-insensitive lenses based on dielectric metasurfaces with meta-molecules. *Optica* **3**, 628–633 (2016).
- Yu, Y. F. *et al.* High-transmission dielectric metasurface with  $2\pi$  phase control at visible wavelengths. *Laser Photon. Rev.* **9**, 412–418 (2015).
- Aieta, F., Kats, M. A., Genevet, P. & Capasso, F. Multiwavelength achromatic metasurfaces by dispersive phase compensation. *Science* **347**, 1342–1345 (2015).
- Shalaev, M. I. *et al.* High-efficiency all-dielectric metasurfaces for ultracompact beam manipulation in transmission mode. *Nano Lett.* **15**, 6261–6266 (2015).
- Arbabi, A., Horie, Y., Bagheri, M. & Faraon, A. Dielectric metasurfaces for complete control of phase and polarization with subwavelength spatial resolution and high transmission. *Nat. Nanotech.* **10**, 937–943 (2015).
- Kamali, S. M., Arbabi, A., Arbabi, E., Horie, Y. & Faraon, A. Decoupling optical function and geometrical form using conformal flexible dielectric metasurfaces. *Nat. Commun.* **7**, 11618 (2016).
- Chong, K. E. *et al.* Efficient polarization-insensitive complex wavefront control using Huygens' metasurfaces based on dielectric resonant meta-atoms. *ACS Photon.* **3**, 514–519 (2016).
- Khorasaninejad, M., Ambrosio, A., Kanhaiya, P. & Capasso, F. Broadband and chiral binary dielectric meta-holograms. *Sci. Adv.* **2**, e1501258 (2016).

54. Zhao, W. *et al.* Full-color hologram using spatial multiplexing of dielectric metasurface. *Opt. Lett.* **41**, 147–150 (2016).
55. Backlund, M. P. *et al.* Removing orientation-induced localization biases in single-molecule microscopy using a broadband metasurface mask. *Nat. Photon.* **10**, 459–463 (2016).
56. Park, S. *et al.* Subwavelength silicon through-hole arrays as an all-dielectric broadband terahertz gradient index metamaterial. *Appl. Phys. Lett.* **105**, 091101 (2016).
57. Kim, S. W., Yee, K. J., Abashin, M., Pang, L. & Fainman, Y. Composite dielectric metasurfaces for phase control of vector field. *Opt. Lett.* **40**, 2453–2456 (2015).
58. Niv, A., Biener, G., Kleiner, V. & Hasman, E. Manipulation of the Pancharatnam phase in vectorial vortices. *Opt. Express* **14**, 4208–4220 (2006).
59. Lalanne, P. Waveguiding in blazed-binary diffractive elements. *Opt. Express* **16**, 2517–2520 (1999).
60. Chong, K. E. *et al.* Polarization-independent silicon metadevices for efficient optical wavefront control. *Nano Lett.* **15**, 5369–5374 (2015).
61. Shcherbakov, M. R. *et al.* Enhanced third-harmonic generation in silicon nanoparticles driven by magnetic response. *Nano Lett.* **14**, 6488–6492 (2014).
62. Yang, Y. *et al.* Nonlinear Fano-resonant dielectric metasurfaces. *Nano Lett.* **15**, 7388–7393 (2015).
63. Shcherbakov, M. R. *et al.* Nonlinear interference and tailorable third-harmonic generation from dielectric oligomers. *ACS Photon.* **2**, 578–582 (2015).
64. Shcherbakov, M. R. *et al.* Ultrafast all-optical switching with magnetic resonances in nonlinear dielectric nanostructures. *Nano Lett.* **15**, 6985–6990 (2015).
65. Makarov, S. *et al.* Tuning of magnetic optical response in a dielectric nanoparticle by ultrafast photoexcitation of dense electron-hole plasma. *Nano Lett.* **15**, 6187–6192 (2015).
66. Campen, R. K. *et al.* Subcycle control of terahertz waveform polarization using all-optically induced transient metamaterials. *Light Sci. Appl.* **3**, e155 (2014).
67. Mezzapesa, F. P. *et al.* Photo-generated metamaterials induce modulation of CW terahertz quantum cascade lasers. *Sci. Rep.* **5**, 16207 (2015).
68. Karvounis, A., Ou, J., Wu, W., Macdonald, K. F. & Zheludev, N. I. Nano-optomechanical nonlinear dielectric metamaterials. *Appl. Phys. Lett.* **107**, 191110 (2016).
69. Kamali, S. M., Arbabi, E., Arbabi, A., Horie, Y. & Faraon, A. Highly tunable elastic dielectric metasurface lenses. *Laser Photon. Rev.* **10**, 1002–1008 (2016).
70. Andryeuskii, A., Lavrinenko, A. V. & Zhukovsky, S. V. Anomalous effective medium approximation breakdown in deeply subwavelength all-dielectric photonic multilayers. *Nanotechnology* **26**, 184001 (2015).
71. Lehmann, V., Stengl, R. & Luigart, A. On the morphology and the electrochemical formation mechanism of mesoporous silicon. *Mater. Sci. Eng. B* **69–70**, 11–22 (2000).
72. Schilling, J. *et al.* A model system for two-dimensional and three-dimensional photonic crystals: macroporous silicon. *J. Opt. A Pure Appl. Opt.* **3**, S121–S132 (2001).
73. Vasi, B. & Isi, G. Controlling electromagnetic fields with graded photonic crystals in metamaterial regime. *Opt. Express* **18**, 20321–20333 (2010).
74. Pap, A. E. *et al.* Optical properties of porous silicon. Part III: comparison of experimental and theoretical results. *Opt. Mater. (Amst.)* **28**, 506–513 (2006).
75. Golovan, L. A., Kashkarov, P. K. & Timoshenko, V. Y. Form birefringence in porous semiconductors and dielectrics: a review. *Crystallogr. Rep.* **52**, 672–685 (2007).
76. Golovan, L. A. *et al.* Phase matching of second-harmonic generation in birefringent porous silicon. *Appl. Phys. B* **73**, 31–34 (2001).
77. Barth, D. S. *et al.* Macroscale transformation optics enabled by photoelectrochemical etching. *Adv. Mater.* **27**, 6131–6136 (2015).
78. Di Falco, A., Kehr, S. C. & Leonhardt, U. Luneburg lens in silicon photonics. *Opt. Express* **19**, 5156–5162 (2011).
79. Hunt, J. *et al.* Planar, flattened Luneburg lens at infrared wavelengths. *Opt. Express* **20**, 1706–1713 (2012).
80. Gabrielli, L. H., Liu, D., Johnson, S. G. & Lipson, M. On-chip transformation optics for multimode waveguide bends. *Nat. Commun.* **3**, 1217 (2012).
81. Zentgraf, B. T., Valentine, J., Tapia, N. & Li, J. An optical “Janus” device for integrated photonics. *Adv. Mater.* **22**, 2561–2564 (2010).
82. Gabrielli, L. H., Cardenas, J., Poitras, C. B. & Lipson, M. Silicon nanostructure cloak operating at optical frequencies. *Nat. Photon.* **3**, 461–463 (2009).
83. Gabrielli, L. H. & Lipson, M. Transformation optics on a silicon platform. *J. Opt.* **13**, 24010 (2011).
84. Tamma, V. A., Blair, J., Summers, C. J. & Park, W. Dispersion characteristics of silicon nanorod based carpet cloaks. *Opt. Express* **18**, 25746–25756 (2010).
85. Spadoti, D. H., Gabrielli, L. H., Poitras, C. B. & Lipson, M. Focusing light in a curved-space. *Opt. Express* **18**, 3181–3186 (2010).
86. Bock, P. J. *et al.* Subwavelength grating periodic structures in silicon-on-insulator: a new type of microphotonic waveguide. *Opt. Express* **18**, 20251–20262 (2010).
87. Cheben, P., Xu, D.-X., Janz, S. & Densmore, A. Subwavelength waveguide grating for mode conversion and light coupling in integrated optics. *Opt. Express* **14**, 4695–4702 (2006).
88. Bock, P. J. *et al.* Subwavelength grating crossings for silicon wire waveguides. *Opt. Express* **18**, 16146–16155 (2010).
89. Halir, R. *et al.* Recent advances in silicon waveguide devices using sub-wavelength gratings. *IEEE J. Sel. Top. Quant. Electron.* **20**, 8201313 (2014).
90. Frandsen, L. H. *et al.* Topology optimized mode conversion in a photonic crystal waveguide fabricated in silicon-on-insulator material. *Opt. Express* **22**, 8525–8532 (2014).
91. Borel, P. I. *et al.* Imprinted silicon-based nanophotonics. *Opt. Express* **15**, 1261–1266 (2007).
92. Piggott, A. Y. *et al.* Inverse design and demonstration of a compact and broadband on-chip wavelength demultiplexer. *Nat. Photon.* **9**, 374–377 (2015).
93. Shen, B., Wang, P., Polson, R. & Menon, R. An integrated-nanophotonics polarization beamsplitter with  $2.4 \times 2.4 \mu\text{m}^2$  footprint. *Nat. Photon.* **9**, 378–382 (2015).
94. Wu, Q., Turpin, J. P. & Werner, D. H. Integrated photonic systems based on transformation optics enabled gradient index devices. *Light Sci. Appl.* **1**, e38 (2012).
95. Gans, R. & Happel, H. *Zur Optik kolloidaler Metallösungen.* *Ann. Phys.* **29**, 277–300 (1909).
96. Schaefer, C. & Stallwitz, H. *Ein zweidimensionales Dispersionsproblem.* *Ann. Phys.* **50**, 199–221 (1916).
97. Lewin, B. L. The electrical constants of a material loaded with spherical particles. *J. Inst. Electr. Eng.* **94**, 65–68 (1947).
98. Sakurai, T. ‘Artificial matter’ for electromagnetic wave. *J. Phys. Soc. Jpn* **5**, 394–398 (1950).
99. Rybin, M. V. *et al.* Phase diagram for the transition from photonic crystals to dielectric metamaterials. *Nat. Commun.* **6**, 10102 (2015).
100. Huang, X., Lai, Y., Hang, Z. H., Zheng, H. & Chan, C. T. Dirac cones induced by accidental degeneracy in photonic crystals and zero-refractive-index materials. *Nat. Mater.* **10**, 582–586 (2011).
101. Moitra, P. *et al.* Realization of an all-dielectric zero-index optical metamaterial. *Nat. Photon.* **7**, 791–795 (2013).
102. Li, Y. *et al.* On-chip zero-index metamaterials. *Nat. Photon.* **9**, 738–742 (2015).
103. Valdivia-Valero, F. J. & Nieto-Vesperinas, M. Composites of resonant dielectric rods: a test of their behavior as metamaterial refractive elements. *Photon. Nanostruct. Fundam. Appl.* **10**, 423–434 (2012).
104. Rolly, B., Bebey, B., Bidault, S., Stout, B. & Bonod, N. Promoting magnetic dipolar transition in trivalent lanthanide ions with lossless Mie resonances. *Phys. Rev. B* **85**, 245432 (2012).
105. Arbabi, A. *et al.* Miniature optical planar camera based on a wide-angle metasurface doublet corrected for monochromatic aberrations. *Nat. Commun.* **7**, 13682 (2016).
106. Cheben, P. *et al.* Refractive index engineering with subwavelength gratings for efficient microphotonic couplers and planar waveguide multiplexers. *Opt. Lett.* **35**, 2526–2528 (2010).
107. Schriever, C. *et al.* Second-order optical nonlinearity in silicon waveguides: inhomogeneous stress and interfaces. *Adv. Opt. Mater.* **3**, 129–136 (2015).
108. Slobzhanyuk, A. *et al.* Three-dimensional all-dielectric photonic topological insulator. *Nat. Photon.* **11**, 130–136 (2017).
109. Liu, S., Keeler, G. A., Reno, J. L., Sinclair, M. B. & Brener, I. III–V semiconductor nanoresonators — a new strategy for passive, active and nonlinear all-dielectric metamaterials. *Adv. Opt. Mater.* **4**, 1457–1462 (2016).

## Acknowledgements

I.S. gratefully acknowledges financial support by the Thuringian State Government within its ProExcellence initiative (ACP<sup>2020</sup>) and by the German Research Foundation through the Emmy Noether Programme (STA 1426/2-1).

## Additional information

Reprints and permissions information is available online at [www.nature.com/reprints](http://www.nature.com/reprints). Publisher's note: Springer Nature remains neutral with regard to jurisdictional claims in published maps and institutional affiliations. Correspondence should be addressed to J.S.

## Competing financial interests

The authors declare no competing financial interests.